VISCOUS HYPERSTABILIZATION OF DETONATION WAVES IN ONE SPACE DIMENSION

BLAKE BARKER[†], JEFFREY HUMPHERYS[‡], GREGORY LYNG[§], AND KEVIN ZUMBRUN[†]

Key words. Evans function, stability, viscous detonation wave

AMS subject classifications. 35Q35,76L05, 80A32

Abstract. It is a standard practice to neglect diffusive effects in stability analyses of detonation waves. Here, with the aim of quantifying the impact of these oft-neglected effects on the stability characteristics of such waves, we use numerical Evans-function techniques to study the (spectral) stability of viscous strong detonation waves—particular traveling-wave solutions of the Navier–Stokes equations modeling a mixture of reacting gases. Our results show a surprising synergy between the high-activation-energy limit typically studied in stability analyses of detonation waves and the presence of small but nonzero diffusive effects. While our calculations do show a modest delay in the onset of instability in agreement with recently reported calculations by direct numerical simulation of the physical equations, our Evans-function-based approach provides additional spectral information. In particular, for each of the families of detonation waves in our computational domain, we find an unexpected kind of hysteresis in the limit of increasing activation energy; that is, *our calculations suggest that, whenever diffusive effects are present, there is is a return to stability as activation energy is further increased, with unstable eigenvalues returning to the stable complex half plane.*

1. Introduction.

1.1. Viscous detonation waves & stability. A detonation wave is a particular and dramatic kind of combustion wave that arises in the dynamics of mixtures of reacting gases. These distinctive waves are characterized by their high speed, substantial energy conversion, and shock-like structure [20]. Indeed, the traditional viewpoint—going back at least to Zel'dovich, von Neumann, and Döring in the 1940s—is that these waves are initiated by a gas-dynamical shock wave (which compresses the gas mixture, heating it and inducing chemical reactions) and their structure is that of a shock wave coupled to and supported by a burning tail [17, 20]. In order to correctly describe the dynamics, it is necessary to properly model the interaction of the combustion processes and the nonlinear behavior of the gas mixture. A standard tenet of the Zel'dovich–von Neumann–Döring (ZND) theory is that diffusive effects[1] can be safely neglected as negligible relative to the more significant reaction and convection effects which are expected to dominate behavior [17, 20, 46]. Indeed, it is a standard practice to model detonations using the (inviscid) reactive Euler/ZND equations [9]. However, questions about the validity of the inviscid approximation go back at least to the 1950s

---

[1]These are the effects of viscosity, heat conductivity, and species diffusion. By an abuse of language, we frequently refer to the collection of all of these effects as the *viscous effects* or simply the *viscosity*.

[26] and figured into the work of Fickett & Davis [20]. More recently, Gardner [22], Gasser & Szmolyan [23], and Williams [47] have all established—under various technical assumptions—the existence of steady detonation waves with viscosity. Gasser & Szmolyan give a rather complete treatment of the existence problem in the limit of vanishing viscosity; the existence problem for larger viscosities is largely untreated and seems to require numerical continuation. Notable mathematical progress towards a stability theory for these waves can be found in the work of Tan & Tesei [44]; Lyng & Zumbrun [36]; Jenssen, Lyng, & Williams [32]; Lyng, Raoofi, Texier, & Zumbrun [35]; Texier & Zumbrun [45]; and Zumbrun [50]. Complementing this theoretical work, the important recent numerical calculations of Romick, Aslan, & Powers [40, 41] form an important foundation for our study. (Earlier calculations of Colella, Majda, & Roytburd [16] and of Bourlioux, Majda, & Roytburd [10] discuss the effect of *numerical* viscosity on the simulation of detonation phenomena.)

The first substantive investigation of the linear stability of detonation waves was initiated by Erpenbeck [18, 19] during the 1960s; Erpenbeck's program for analyzing the stability of ZND detonation waves is described in detail in the text of Fickett & Davis [20], and it forms the foundation on which subsequent work in this area has been built. For example, Lee & Stewart [34], still in the ZND setting, considerably clarified the theory by providing a far more complete description of the neutral stability boundaries in parameter space. Here, continuing the Evans-function program initiated by Lyng & Zumbrun [36], we examine, by numerically computing the relevant Evans function, the stability of strong-detonation-wave solutions of the Navier–Stokes equations modeling a mixture of reacting gases. The Evans function, $\mathbb{E}$—an analytic function of a complex spectral parameter λ, is a "stability function" analogous to the stability function introduced by Erpenbeck [18, 19] for the ZND system; it is constructed so that its zeros in the unstable complex half plane signal the presence of perturbations that grow exponentially in time. That is, the zeros of $\mathbb{E}$ coincide in location and multiplicity with the eigenvalues of the linearized operator about the wave. Indeed, $\mathbb{E}$ is a central element in a general framework for stability analysis (which includes, for example, the stability function of Erpenbeck as a special case), see e.g. [42, 48]. On the one hand, $\mathbb{E}$ can be viewed in an operator-theoretic sense as a Fredholm characteristic determinant. This point of view has a great deal of utility in theoretical approaches to nonlinear stability analysis. On the other hand, $\mathbb{E}$ can be evaluated, using shooting methods, as a Wronskian of solutions of differential equations. It is this latter feature that is important here. However, although shooting may appear to be straightforward, a number of algorithms/techniques have been developed recently to address the nontrivial problem of approximating $\mathbb{E}$ for physically interesting systems [12, 13, 29, 30, 49]. These techniques have been used to analyze the stability of viscous shock profiles in gas dynamics [4, 27] and for detonation waves in simplified, scalar models [7, 28, 24]. Here, we extend these techniques to the physically relevant, computationally challenging setting of the Navier–Stokes equations, system (2.1). Indeed, despite the voluminous data on ZND spectra, we know of no similar calculations for Navier–Stokes systems. Thus, the quantitative comparisons obtained here open a new line of investigation.

1.2. Description of results: viscous hyperstabilization. We describe the principal results of our computations. To start, we outline the steps required to approximate $\mathbb{E}$ for a given detonation wave. The first step is to approximate the wave itself. As a traveling-wave solution of the Navier–Stokes equations (system (2.1)) the viscous structure of the wave is encoded in a nonlinear two-point boundary-value

problem posed on the real line. Said differently, the wave is a heteroclinic orbit in the phase space $\mathbb{R}^4$; the approximation of this orbit is described in §3.6. Once the traveling-wave profile is in hand, we may turn our attention to the computation of $\mathbb{E}$. This computation requires the solution of a nonautonomous linear system of differential equations whose coefficients depend on the wave profile and on λ (see equation (4.1)). Here, we use StabLab, a computational package being developed for this purpose [5], to carry out these calculations. We take care to maintain the analyticity of the Evans function with respect to the spectral parameter; this facilitates the use of winding number calculations to search for zeros (unstable eigenvalues). A more complete description of the methodology for computing $\mathbb{E}$ can be found in §5 and in [12, 13, 29, 30, 49].

With $\mathbb{E}$ in hand, we may systematically search for unstable eigenvalues of the linearized operator. The first task is to determine the shape of the neutral stability boundary and to compare it to the neutral stability boundary, as computed by Erpenbeck and his successors, for the corresponding ZND profiles. For example, Romick et al. [40, 41], using direct numerical simulation of the temporal evolution of the physical system of equations, found that the presence of viscosity delayed the onset of instability by about 10%. We recover this result, but our approach yields more information. In particular, for each of the families of detonation waves in our computational domain, we find an unexpected kind of hysteresis in the limit of increasing activation energy; indeed, our calculations suggest that, whenever diffusive effects are present, as activation energy increases there is a return to stability as unstable eigenvalues return to the stable complex half plane. *We call this behavior **viscous hyperstabilization**, and we conjecture that it persists for all nonzero viscosities.* A particularly interesting feature of these calculations is the growth of the upper-stability boundary in the limit of vanishing viscosity. Results of Zumbrun, together with the numerically observed absence of an upper stability boundary for inviscid case, imply that this boundary must escape to infinity as the viscosity tends to zero [50], but our computations suggest a very slow, perhaps logarithmic, growth, in the stabilizing activation energy as a function of viscosity. See Figure 1. We regard the further investigation of this phenomenon via singular perturbation theory as a fundamental open problem in the theory. Another notable feature of left-hand pane of Figure 1 is the "nose" of the neutral stability curve. That is, for sufficiently large viscosity, the upper and lower boundaries meet indicating no instability regardless of the value of $\mathcal{E}_A$.

1.3. About the computations. We see several noteworthy aspects of these computations which we now describe.

1.3.1. Computational tractability. First, the computation of the Evans function in this physically relevant setting serves as an important, practical validation of the utility of the polar-coordinate ("analytic orthogonalization") technique for approximating the Evans function; see [30] and the references therein, in particular [37]. For context, we recall that the computation of the Evans–Lopatinskiĭ function (essentially Erpenbeck's stability function) for the ZND system is well known to be a computationally intense problem. For more details about the difficulties, we refer the reader to the foundational paper of Lee & Stewart [34] and also to more recent work by Humpherys & Zumbrun [31]. Briefly, however, we can see by a dimension count that the ZND calculation requires the (stiff) computation of a single mode of a 4×4 system while the computation for the equations with viscosity requires one to track 3 growing and 3 decaying solutions of a 7×7 system. Thus, the (assumed small) effects of viscosity are responsible for a considerable increase in the size and complexity of the
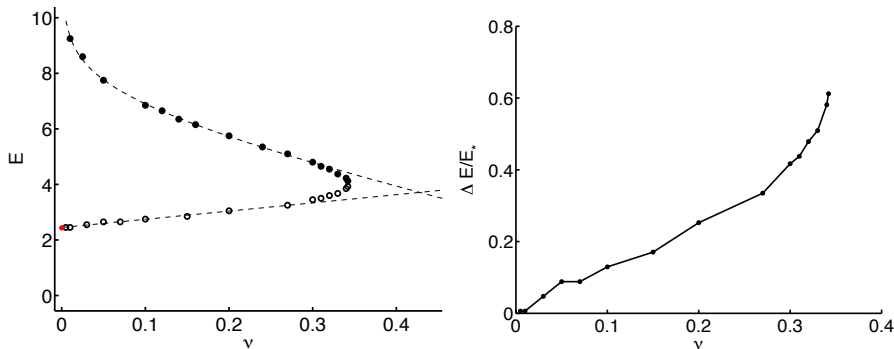
FIG. 1. *LEFT: Neutral Stability Boundaries in the $\mathcal{E}_A$-ν plane. The upper and lower stability boundaries ($\mathcal{E}_A^{\pm}$, see also Tables 2 and 3) are denoted by black dots and circles, respectively; the red dot denotes the ZND (inviscid) stability boundary. The best-fit curve (dashed line, $\nu < 0.27$) for the upper boundary is $\mathcal{E}_A^{+}(\nu) = 5.67 - 6.16\nu - 0.804\ln(\nu)$. For the lower boundary, the best-fit curve (dashed line, $\nu \leq 0.27$) is linear: $\mathcal{E}_A^{-}(\nu) = 2.45 + 2.95\nu$. Here, $\nu = d = \kappa$, $\Gamma = 0.2$, $e_+ = 6.23e\text{-}2$, $q = 6.23e\text{-}1$, and $T_{\mathrm{ig}} = 0.99$. RIGHT: Viscous Delay: We plot $\Delta E/\mathcal{E}_* = (\mathcal{E}_A^{-}(\nu) - \mathcal{E}_*)/\mathcal{E}_*$ against ν, where $\mathcal{E}_*$ is the approximation to the ZND neutral boundary. Here, $\nu = D = \kappa$, $\Gamma = 0.2$, $e_+ = 6.23e\text{-}2$, $q = 6.23e\text{-}1$, and $T_{\mathrm{ig}} = 0.99$*

linearized system. Indeed, when applied to the ZND stability problem, results of [8] suggest the algorithms used in StabLab appear to perform 1-2 orders of magnitude faster than the ones used by [34] (and used more recently in [43]). All numerical investigations were carried out using either a 2009 MacBook with a 2.0 GHz Intel Core 2 Duo processor, a Mac Pro with two Quad-Core Intel Xeon 2.26 GHz processors, or the research cluster Quarry at Indiana University, with Mac processors used mainly for prototyping/debugging purposes and more substantial computations sent as batch jobs to Quarry.

1.3.2. Virtues of the Evans-function approach. One benefit of the Evans-function approach is that it reveals information about the eigenstructure of the linearized operator. For example, as noted above, one of our experiments utilizes the same parameter values as used in the recent studies of Romick et al. [40, 41]. Their computations, however, are based on the direct numerical simulation of the temporal evolution of the governing physical system of partial differential equations. Here, using the same (physically motivated, but somewhat arbitrary) parameters, we find the same 10% delay in the onset of instability as seen by Romick et al. [40, 41]. At first glance, this supports the conventional wisdom that diffusive effects are essentially perturbative. However, as noted above, continuing to follow roots as the activation energy $\mathcal{E}_A$ is increased, we find a return to stability—viscous hyperstabilization; see Figure 4 below. Moreover, rather than the well-known cascade of Hopf bifurcations associated with the stability problem in the ZND setting, *we see only two pairs of complex conjugate roots crossing the imaginary axis into the unstable complex half plane.* Thus, the inclusion of diffusive effects in the model results in striking changes at the spectral level. The mechanism for this behavior appears to be a kind of synergy between viscosity and activation energy. The inviscid limit is highly nonuniform with respect to $\mathcal{E}_A$, and this nonuniformity manifests itself in both the structure of the viscous profiles (see the discussion of "benches" in §3.6.2 below) and subsequently in

eigenvalues[2]. We note that the benching phenomenon appears to occur for a rather pedestrian reason. That is, its origin is due to the different powers of τ, the specific volume, that appear in the viscous terms on the right-hand side in the system (2.1). How this profile structure affects the eigenvalues (or indeed whether this relationship is truly causal as we conjecture here) is an interesting open question, even at heuristic level.

1.3.3. Implications & future work. Finally, these findings may be significant in various applications in certain parameter regimes. For example, we note that instability characteristics of detonation waves are critically relevant in the design of any viable detonation-based propulsion system, a problem which remains largely open [43]. While the implications for applications remain to be explored, these results seem to warrant a more detailed analysis of the viscous system, and Evans-based techniques appear to offer an effective starting point for this endeavor.

2. Equations for reacting mixtures of gases.

2.1. Navier–Stokes equations. In a single spatial dimension (Lagrangian coordinates), the Navier–Stokes equations for a reacting two-species gas mixture take the form (see, e.g., [15])

$$\tag{2.1a} \tau_t - u_x = 0\,,$$

$$\tag{2.1b} u_t + p_x = \left(\frac{\nu u_x}{\tau}\right)_x,$$

$$\tag{2.1c} \left(e + \frac{u^2}{2}\right)_t + (pu)_x = \left(\frac{\nu u u_x}{\tau} + \frac{\kappa T_x}{\tau}\right)_x + qk\phi(T)z\,,$$

$$\tag{2.1d} z_t = -k\phi(T)z + \left(\frac{Dz_x}{\tau^2}\right)_x.$$

Here, subscripts denote partial derivatives (t is time and x is a Lagrangian marker), τ is the specific volume (length), u is the velocity, p is the pressure, and $z \in [0,1]$ is the mass fraction of reactant. The positive constants ν, κ, and D represent viscosity, heat conductivity, and species diffusivity respectively. The constant $k > 0$ is the collision frequency constant, and q measures the difference in the heats of formation in the reactant and the product. That is, it is a measure of the amount of energy released during the reaction process. We assume $q > 0$ which corresponds to an exothermic reaction. The function ϕ is the ignition function; it serves as an on/off switch for the reaction. Finally, T is the temperature, and we assume initially that the internal energy e and the pressure p are known functions of the specific volume, the temperature, and the mixture of the product and reactant gases: $p = p_0(\tau, T, z)$, $e = e_0(\tau, T, z)$. We describe the functions p_0 and e_0 in §2.2. A detailed discussion of such Navier–Stokes systems for reacting mixtures can be found in Williams [46]. For brevity, we refer to the system (2.1) as the RNS system or as the RNS equations.

REMARK 1 (Eulerian vs. Lagrangian). *We work in Lagrangian coordinates. Our experiments suggest that, for viscous shock profiles in gas dynamics, the Evans function arising from the Lagrangian system is considerably better behaved than it's Eulerian counterpart; indeed, we have found that Evans-function computation in the Lagrangian framework can be faster by two or more orders of magnitude.*

---

[2]We recall the paradigm of Henry [25]: essential spectrum corresponds to far-field behavior while point spectrum (located by $\mathbb{E}$) arises from the detailed structure of the shock layer/reaction zone.

2.2. Equations of state & ignition.

2.2.1. Ideal gas. The simplest case of interest occurs when we consider an ideal, polytropic gas. In this case the energy and pressure functions take the specific form

$$(2.2) \qquad p_0(\tau, T, z) = \frac{RT}{\tau}, \quad e_0(\tau, T, z) = c_v T,$$

where $R \geq 0$ and $c_v > 0$ are constants that characterize the gas. Alternatively, we can write the pressure in terms of the internal energy and the specific volume as $p = \Gamma e/\tau$, where $\Gamma = \gamma - 1 = \frac{R}{c_v} \geq 0$, $\gamma \geq 1$ the gas constant. We note that due to (2.2), the specific internal energy is simply a multiple of the temperature, and these two quantities can effectively be used interchangeably.

2.2.2. Ignition function. We assume that ϕ is of the Arrhenius form with an ignition temperature cut-off at a distinguished threshold temperature T_{ig}. That is, we assume

$$(2.3) \qquad \phi(T) = \begin{cases} \exp\left(-\mathcal{E}_A/[c_v(T - T_{ig})]\right), & \text{if } T \geq T_{ig} \\ 0, & \text{otherwise} \end{cases}$$

with $\mathcal{E}_A$ the activation energy and T_{ig} the ignition temperature. (Although qualitatively similar, we note that this form of ϕ differs from that used in [41].) Using the relationship $e = c_v T$, we sometimes write $\check{\phi}(e) = \phi(T)$. For our numerical experiments we choose the ignition value of the specific internal energy, $e_{ig} := c_v T_{ig}$, to be a convex combination of the end state e_+ and e_{mid}—defined to be the value of the specific internal energy at $x = 0$ (at the jump) in the corresponding ZND solution. The convex combination is weighted heavily to favor the contribution of the unburned state e_+.

3. Traveling-wave profiles & scaling.

3.1. Traveling waves. The viscous strong detonation waves that are the focus of our analysis are traveling-wave solutions of (2.1). Suppose that $(\tau, u, e, z)(t, x) = (\hat{\tau}, \hat{u}, \hat{e}, \hat{z})(x - st)$ is a traveling-wave solution connecting constant states $(\tau_\pm, u_\pm, e_\pm, z_\pm)$. Our interest is in waves connecting an unburnt state $(z_+ = 1)$ to a completely burnt state $(z_- = 0)$.

3.2. A convenient scaling. Evidently, a traveling-wave solution is a stationary solution of the system

$$(3.1a) \qquad \tau_t - s\tau_x - u_x = 0,$$

$$(3.1b) \qquad u_t - su_x + p_x = \left(\frac{\nu u_x}{\tau}\right)_x,$$

$$(3.1c) \qquad \left(e + \frac{u^2}{2}\right)_t - s\left(e + \frac{u^2}{2}\right)_x + (pu)_x = \left(\frac{\nu u u_x}{\tau} + \frac{\kappa_v e_x}{\tau}\right)_x + qk\check{\phi}(e)z,$$

$$(3.1d) \qquad z_t - sz_x = -k\check{\phi}(e)z + \left(\frac{Dz_x}{\tau^2}\right)_x.$$

We scale the independent variables using $L > 0$ as

$$(3.2) \qquad x \to \frac{\tau_+ sx}{L} =: \bar{x}, \quad t \to \frac{\tau_+ s^2 t}{L} =: \bar{t},$$

and we scale the dependent variables as

(3.3)
$$\tau \to \frac{\tau L}{\tau_+} =: \bar\tau \,, \quad u \to \frac{uL}{\tau_+ s} =: \bar u \,, \quad e \to \frac{L^2 e}{\tau_+^2 s^2} =: \bar e \,.$$

Then, with $\bar u(\bar t(t), \bar x(x)) = \frac{Lu(t,x)}{\tau_+ s}$ and so forth, the equations in barred variables read

(3.4a)
$$\bar\tau_{\bar t} - \bar\tau_{\bar x} - \bar u_{\bar x} = 0 \,,$$

(3.4b)
$$\bar u_{\bar t} - \bar u_{\bar x} + \bar p_{\bar x} = \left(\frac{\nu \bar u_{\bar x}}{\bar\tau} \right)_{\bar x} \,,$$

(3.4c)
$$\left(\bar e + \frac{\bar u^2}{2} \right)_t - \left(\bar e + \frac{\bar u^2}{2} \right)_x + (\bar p \bar u)_{\bar x} = \left(\frac{\nu \bar u \bar u_{\bar x}}{\bar\tau} + \frac{\kappa_\nu \bar e_{\bar x}}{\bar\tau} \right)_x + \bar q \bar k \bar{\breve\phi}(\bar e) \bar z \,,$$

(3.4d)
$$\bar z_{\bar t} - \bar z_{\bar x} = -\bar k \bar{\breve\phi}(\bar e) \bar z + \left(\frac{D \bar z_{\bar x}}{\bar\tau^2} \right)_{\bar x} \,.$$

In (3.4), we have used

$$\bar{\breve\phi}(\bar e) = \breve\phi \left(\frac{\tau_+ s}{L^2} \bar e \right) \,, \quad \bar k = \frac{kL}{\tau_+ s^2} \,, \quad \bar q = \frac{qL^2}{\tau_+ s^2} \,.$$

Remarkably, the pressure law is *unchanged* in this new formulation; for further discussion see [27]. Henceforth, we drop the bars. Evidently, the profile is determined by the system of ordinary differential equations obtained by neglecting the time-derivative terms in (3.4). Using (from the scaling and translation invariance) $s = 1 \,, \tau_+ = 1, \, u_+ = 0$, and the ideal gas pressure law, and integrating once, we may write the result as a first-order system with $y := \frac{D z'}{\tau^2}$ where $' = \mathrm{d}/\mathrm{d}x$. The result is

(3.5a)
$$\tau' = -\frac{1}{\nu} \left[\tau(\tau - 1) + \Gamma(e - e_+ \tau) \right] \,,$$

(3.5b)
$$e' = -\frac{\tau}{\kappa_v} \left[\frac{(\tau - 1)^2}{2} + (e - e_+) + \Gamma e_+ (\tau - 1) + q(y + z - z_+) \right] \,,$$

(3.5c)
$$z' = D^{-1} \tau^2 y \,,$$

(3.5d)
$$y' = k \breve\phi(e) z - D^{-1} \tau^2 y \,.$$

In system (3.5), we have used the conservation of mass equation to eliminate the velocity u from the system; of course, the velocity u and the specific volume τ are related by the simple relation $u = 1 - \tau$, and we have used the following convenient notation $\kappa_v := \kappa/c_v$. There are three equilibria of this system, and their nature determines the type of connecting orbit (e.g., strong detonation or weak detonation). See [23] for further details. A key point for the calculations in this paper is that the connecting orbit problem for strong detonations is numerically well conditioned due to the transverse intersection of stable/unstable manifolds.

3.3. Parametrization. Summing up, we may take without loss of generality $s = 1, \, \tau_+ = 1$ and (by translation invariance in u), $u_+ = 0$, leaving $e_+ > 0$ as the parameter determining the wave. By explicit computation using the Rankine–Hugoniot relations ([50], Appendix C), we have then that the burned end state is given by
(3.6)
$$\tau_- = \frac{(\Gamma + 1)(\Gamma e_+ + 1) - \sqrt{(\Gamma + 1)^2 (\Gamma e_+ + 1)^2 - \Gamma(\Gamma + 2)(1 + 2(\Gamma + 1)e_+ + 2q))}}{\Gamma + 2} \,,$$

where

$$(3.7) \qquad u_- = 1 - \tau_- , \quad e_- = \frac{\tau_-(\Gamma e_+ + 1 - \tau_-)}{\Gamma},$$

and q satisfies $0 \leq q \leq q_{\mathrm{CJ}}$ with

$$(3.8) \qquad q_{\mathrm{CJ}} := \frac{(\Gamma + 1)^2 (\Gamma e_+ + 1)^2 - \Gamma(\Gamma + 2)(1 + 2(\Gamma + 1)e_+)}{2\Gamma(\Gamma + 2)}.$$

Thus, we can parametrize all possible profiles by

$$(3.9) \qquad (e_+, q, \mathcal{E}_A, \Gamma, \nu, D, \kappa_v, k),$$

where $0 \leq e_+ \leq \frac{1}{\Gamma(\Gamma + 1)}$, $0 \leq q \leq q_{\mathrm{CJ}}(e_+)$, $0 \leq \mathcal{E}_A < \infty$, and $0 < \Gamma < \infty$. By a further common rescaling of space and time, we can fix k at any desired value. Following standard practice, we shall choose the value of k so that the reaction zone of the associated inviscid (ZND) profile is of roughly constant length; more precisely, to match corresponding ZND computations done previously in [8]. In particular, we choose k so that the corresponding ZND (inviscid) solution with this ignition function has the value $z = 1/2$ at $x = -10$ in the spatial domain; the jump is at $x = 0$. See [50] for further details.

3.4. The high-overdrive limit and the scaling of Erpenbeck. A similar scaling was used by Erpenbeck in [18, 19], but with e_+ held fixed instead of wave speed s. As pointed out previously [27, 50], the advantage of our choice is that the coefficients of the linearized eigenvalue equations remain bounded in the limit of increasing strength of the Neumann shock. Converting from Erpenbeck's to our scaling amounts to rescaling the wave speed, so that $T \to T/s^2$ and $\mathcal{E}_A \to \mathcal{E}_A/s^2$, and $t \to ts^2$ (u is translation invariant, so irrelevant). Thus, as noted by Zumbrun [50], the high-overdrive limit discussed by Erpenbeck [18], in which $s \to \infty$ with u_+ held fixed, corresponds in our scaling to taking $\mathcal{E}_A = \mathcal{E}_0 e_+$, $q = q_0 e_+$, and varying e_+ from $e_+ = e_{\mathrm{CJ}}(q_0)$ (s minimum) to 0 ($s = \infty$). Here, the value of e_{CJ} may be obtained from the relation $q_{\mathrm{CJ}}(e_{\mathrm{CJ}}) = q_0 e_{\mathrm{CJ}}$. This is the simultaneous *zero heat release, zero activation energy*, and *strong shock limit* ($e_+ \to 0$, $\mathcal{E}_A \to 0$, and $q \to 0$). To complete the translation from Erpenbeck's coordinatization to ours, and back, we must compute the overdrive, which Erpenbeck uses in place of our e_+ to complete the description of the wave (recall that he holds e_+ fixed at value 1). The overdrive is defined for fixed q_0 and $\tau_+ = e_+ = 1$, as $\mathsf{f} := M^2/M_{\mathrm{CJ}}^2$, where M is the Mach number and M_{CJ} is the Mach number of the detonation with same right end state and q_0, but traveling with CJ speed. In the present setting (the scaling introduced above), we must therefore compute the Mach number for a detonation with $q = q_0 e_+^{\mathrm{CJ}}$, $\tau_+ = 1$, and $q_{\mathrm{CJ}}(e_+^{\mathrm{CJ}}) = q_0 e_+^{\mathrm{CJ}}$, or

$$(3.10) \qquad q_0 e_+^{\mathrm{CJ}} = \frac{(\Gamma + 1)^2 (\Gamma e_+^{\mathrm{CJ}} + 1)^2 - \Gamma(\Gamma + 2)(1 + 2(\Gamma + 1)e_+^{\mathrm{CJ}})}{2\Gamma(\Gamma + 2)}.$$

Thus, for e_+^{CJ} small, this gives asymptotically $e_+^{\mathrm{CJ}} \sim (2\Gamma(\Gamma + 2)q_0)^{-1}$, hence, noting that $q_0 = q/e_+$, we find that

$$(3.11) \qquad \mathsf{f} = \frac{e_+^{\mathrm{CJ}}}{e_+} \sim \frac{1}{2\Gamma(\Gamma + 2)q},$$

where $q \lesssim \frac{1}{2\Gamma(\Gamma+2)}$. Taking the limit all the way to $e_+ = 0$, we may thus estimate f simply in terms of q, via (3.11).

EXAMPLE 1. *For example, $e_+ = 0$, $q = 0.1$, $\Gamma = 0.2$ gives $\mathsf{f} \approx 11.3$, but q_0, $\mathcal{E}_0 \to \infty$.*

EXAMPLE 2 (Benchmark). *To duplicate Fickett and Wood's [21] benchmark problem $q_0 = \mathcal{E}_0 = 50$, $\Gamma = 0.2$, we take $e_+^{\mathrm{CJ}} \sim \frac{1}{2\Gamma(\Gamma+2)q_0} \approx .023$, and vary $\mathcal{E} = \mathcal{E}_0 e_+ = 50 e_+$, $q = q_0 e_+ = 50 e_+$ as e_+ varies between e_+^{CJ} and 0, with $1 \leq \mathsf{f} = e_+^{\mathrm{CJ}}/e_+ < +\infty$. Here, we expect (and find) the onset of instability around $\mathsf{f} \approx 1.73$, or $e_+ \approx .012$, $q \approx (.012)(50) = .6$, $\mathcal{E}_A = .6$. Results for this problem have now been duplicated by direct numerical simulation, evaluation of the Evans–Lopatinskiĭ function (ZND) by Lee & Stewart [34], and now by numerical computation of the Evans function (RNS) here. Thus, there are now multiple independently computed sources confirming this behavior.*

3.5. Viscous scaling. To determine appropriate ranges for the viscous parameters in our model, we use—as in related studies [40, 41]—the ratio of width of the viscous shock layer to the length of the reaction zone. That is, we choose the reaction rate k (as discussed above in §3.3) to hold the length of reaction zone constant, and then we vary ν, κ, and D to adjust the width of the shock layer. The key observation is that the ratio of shock to reaction width is independent of the rescalings we have performed above. As a starting point, we adopt the ratio of Romick et al. [41] in which the ratio of length scales is $1/10$. As noted there, this ratio is an order of magnitude too big to be physical; indeed, Powers & Paolucci have shown that a large range of length scales are important in realistic models (including detailed chemical kinetics) [39]. Thus, our experiments include a range of ratios including $1/10$, but we also compute closer to the inviscid limit; see Figure 1. For example, visual inspection of Figure 2 shows a ratio of approximately $1/10$.

3.6. Approximation of profiles and phenomenology.

3.6.1. Computational protocol. To approximate a detonation profile (a heteroclinic orbit of (3.5) in $\mathbb{R}^4$ connecting equilibria $(\tau_\pm, e_\pm, z_\pm, y_\pm)$), we must solve a nonlinear two-point boundary-value problem posed on the whole real line. First, we truncate the problem to a finite computational domain $[-M_-, M_+]$ for $M_\pm > 0$, and we supply appropriate projective boundary conditions at $\pm M_\pm$. Finally, we use MATLAB's boundary-value solver, an adaptive Lobatto quadrature scheme, to compute the approximate profile. A frequent challenge associated with this approach is the need to supply an adequate initial guess to the boundary-value solver to seed a Newton iteration. Because of this, the ability to continue solutions as parameter values change is an important art. In fact, we sometimes took steps in $\mathcal{E}_A$ as small as 10^{-4} for small viscosity (0.008) when approximating the profile. To initiate the process, we used a ZND profile as the initial guess, and then we used continuation to fill out parameter space. Finding the profiles was by far the most challenging aspect of these computations. Additionally, to ensure that the profile is completely resolved in the domain, the values for $M_\pm$, must be chosen with some care. Writing the traveling-wave equation (3.5) as $\hat{U}' = F(\hat{U})$ together with the condition that $\hat{U} \to U_\pm$ as $\xi \to \pm\infty$, the typical requirement is that $M_\pm$ should be chosen so that $|\hat{U}(\pm M_\pm) - U_\pm|$ is within a prescribed tolerance of 1e-4. We also set the relative and absolute error tolerances for the boundary-value solver to be 1e-6 and 1e-8 respectively.

3.6.2. "Benches". An example illustrating the solution of (3.5) is shown in Figure 2. The figure compares the viscous solution to the ZND solution connecting the same end states. One interesting result of these computations regards the behavior of the z component. In particular, visually, the deviation of the RNS z profile from the limiting ZND profile is quite striking relative to that of the other components of the solution. This discrepancy is particularly pronounced near the shock layer. As shown in Figure 2, the z profile hits the shock layer at a height below $z = 1$ and makes a near vertical adjustment in the shock layer to achieve the correct limiting value. We call this feature of the traveling wave a "bench," and we saw benches of various sizes for all of the positive viscosity values tested. Further investigation reveals that the bench formation appears to be, more or less, a result of the distinct diffusive scalings in the traveling-wave equation. We note that the diffusivities scale like 1 in (3.5a), τ in (3.5b), and τ^2 in (3.5c) and (3.5d) and that the value of τ is actually rather small for the profiles involved in our computations (roughly 0.15 in Figure 2). Thus, the diffusivities range over several orders of magnitude.
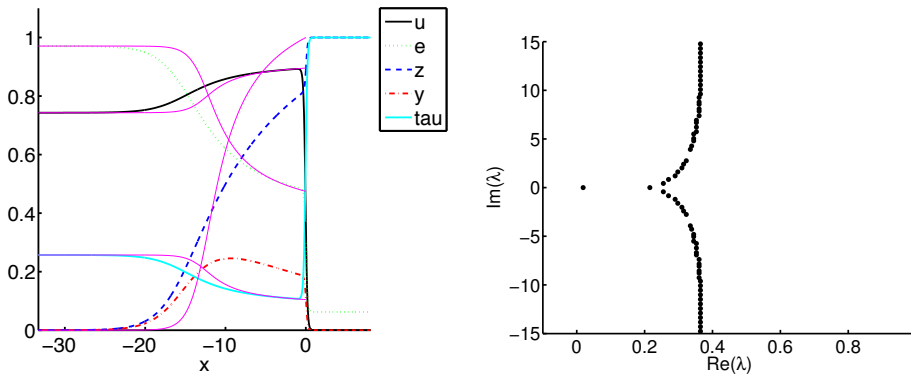

FIG. 2. *(Color online) LEFT: RNS profile vs. ZND profile. The legend shows the values of the velocity (u), specific internal energy (e), mass fraction of reactant (z), y, and specific volume (τ). The thin (magenta) lines denote the components of the corresponding ZND solution. The discrepancy between the z profiles is especially pronounced near the shock layer (close to $x = 0$). Here, $e_+ = 6.23e\text{-}2$, $k = 2.71e\text{-}1$, $d=0.1$, $\nu=0.1$, $\kappa=0.1$, $q=6.23e\text{-}1$, $\mathcal{E}_A=3.1$, $\Gamma=0.2$, $c_v=1$. RIGHT: Unstable eigenvalues in the complex plane for the inviscid/ZND problem. The activation energy is $\mathcal{E}_A = 7.1$ and all of the other parameter are as in Figure 4. This figure is taken from [8] (with permission of the authors); details of the computational method may be found in [8, 7].*

4. Linearization & Evans function. Here, we outline the basics steps in the construction of the Evans function. The first step is to linearize the system (3.1) about the steady strong-detonation profile. Taking the Laplace transform with respect to time, we obtain the eigenvalue problem for the linearized operator. For the completeness, we detail these computations in §A. The upshot is the we obtain a linear, first-order system of ODEs with coefficients depending on x and λ. We write this system as

$$(4.1) \qquad\qquad \mathcal{W}' = G(x;\lambda)\mathcal{W}, \quad ' = \mathrm{d}/\mathrm{d}x,$$

and we note that $\mathcal{W} \in \mathbb{C}^7$ and the coefficient matrix G is a 7×7 matrix. Moreover, since the wave profile tends to constant states at $\pm\infty$, there is an associated pair of limiting constant-coefficient systems: $\mathcal{Z}' = G_\pm(\lambda)\mathcal{Z}$ where $G_\pm(\lambda) := \lim_{x\to\pm\infty} G(x;\lambda)$.
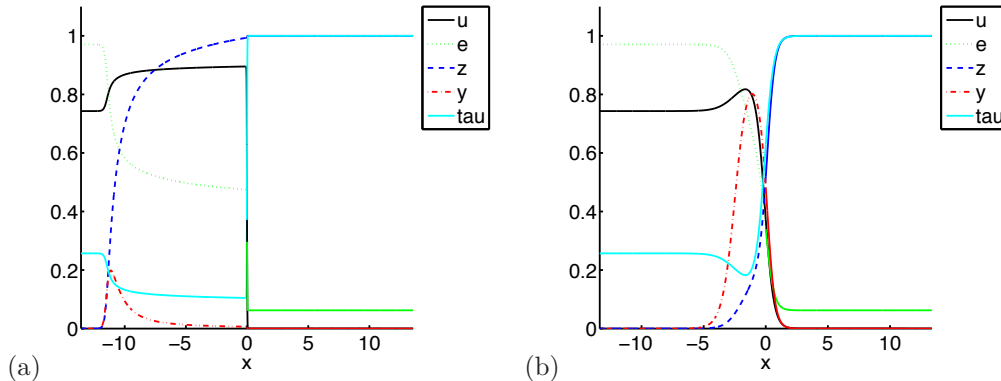
Fig. 3. *Sample profiles illustrating diffusive effects. (a) $\nu = D = \kappa = 0.01$. (b) $\nu = D = \kappa = 0.3$. In both cases the reaction zone structure is clearly visible, but in (b) the shock width is of a similar order as the reaction zone width. For both plots, $T_{ig} = 6.64e\text{-}2$, $e_+ = 6.23e\text{-}2$, $k = 1.53e4$, $q = 6.23e\text{-}1$, $\mathcal{E}_A = 6$, $\Gamma = 0.2$, $c_v = 1$.*

The Evans function $\lambda \mapsto \mathbb{E}(\lambda)$ is computed from the system (4.1). Detailed descriptions of the (theoretical) construction of the Evans function for the RNS equations can be found in [36, 32]. Here we simply note that, if $\mathbb{W}^{\pm}(\lambda)$ are the vector spaces consisting of data at $x = 0$ for which solutions of (4.1) decay to zero at $\pm\infty$, then the Evans function may be defined for $\operatorname{Re}\lambda > 0$, up to nonvanishing factors, by

$$(4.2) \qquad \mathbb{E}(\lambda) := \det\left(\mathbb{W}^+(\lambda), \mathbb{W}^-(\lambda)\right).$$

(The dimensions of $\mathbb{W}^{\pm}$ work out so that the determinant makes sense.) Thus, the task of approximating $\mathbb{E}$ amounts to computing analytic bases for $\mathbb{W}^{\pm}(\lambda)$. Roughly, these bases are found by integrating (4.1) toward the origin from $\pm\infty$ (using explicitly calculable information from $G_{\pm}$ to initialize the computation).

5. Methodology. There is now an established and growing literature describing various techniques for the numerical approximation of the Evans function; see, e.g., [12, 29, 30, 5]. We describe the steps.

Step #1. Approximation of the viscous profile Described in §3.6.1.

Step #2. Approximation of the Evans function As noted earlier, the evaluation of $\mathbb{E}$ is accomplished by means of the STABLAB package, a MATLAB-based package being developed for this purpose [5]. This package allows the user to choose to approximate the Evans function either via exterior products, as in [3, 12, 2], or by a polar-coordinate ("analytic orthogonalization") method [30], which is used here. Because analyticity of the Evans function is one of its essential properties, we use Kato's method [33] to analytically determine the relevant initializing eigenvectors; see [13, 11, 29] for details. Throughout our study, we set the relative and absolute error tolerances on MATLAB's ODE solver `ode45` to be 1e-6 and 1e-8 respectively.

Step #3. Bound on unstable eigenvalues We obtain a numerical upper bound R on the maximum modulus of unstable eigenvalues by testing convergence to relative error 0.2 on a semicirlcle of radius R to theoretically-predicted high-frequency asymptotics $\mathbb{E}(\lambda) \sim C_1 e^{C_2\sqrt{\lambda}}$ as described in [27, 7, 8].

Step #4. Winding & roots Our approach to finding roots of $\mathbb{E}$ on the finite set $B_R \cap \{\operatorname{Re}\lambda \geq 0\}$ is based on the method of moments described in, e.g.,

[14, 6]. Being fundamentally based on Rouché's theorem, this technique takes advantage of the analyticity of the Evans function. Unlike Newton-based, iterative methods for root finding, this approach requires neither a good initial guess for the root location nor excessive evaluations of the function $\mathbb{E}$. These features make this approach attractive, and they provide justification for the care taken above to ensure analyticity. For the RNS system, we use the method of moments in conjunction with a two-dimensional bisection method to locate zeros of $\mathbb{E}$.

Step #5. Neutral stability boundaries Finally, we determine neutral stability curves by bisection in $\mathcal{E}_A$, bracketing between values with nonzero (unstable) and zero (stable) winding number, terminating when relative error, measured as relative difference between the bracketing approximants, is less than a prescribed value.

REMARK 2 (Radius bounds). *At the extreme boundaries of our computational domain, that is, when $\mathcal{E}_A$ is large and ν is small, we were not alway able compute a bound, R, on the size of possible unstable eigenvalues. In this handful of cases, we either used $R = 10$ or took R to be twice the radius needed to bound ZND roots. In some cases this made R very small since near the lower neutral stability boundary, the ZND roots are themselves quite small. However, we emphasize that for our principal experiment mirroring the calculations of Romick et al. [41], we were able to compute bounds for all tested waves, and the resulting values of R are reported in Table 1.*

6. Results: viscous hyperstabilization. We now describe our principal experiments. For various families of viscous strong detonation waves we compute the zeros of the associated Evans functions in the large-$\mathcal{E}_A$ limit. Plots of this spectral information, shown together with the spectral data from the corresponding inviscid ZND profiles gives a direct way to visualize the impact of the viscous terms in the RNS model on the stability of these waves. This is shown in Figure 4. Initially, we find a crossing of a complex conjugate pairs of eigenvalues into the unstable half plane; this signal of a Hopf-type bifurcation is completely expected. However, continuing to follow the eigenvalues as $\mathcal{E}_A$ increases, we find a restabilization.

6.1. The viscosity of Romick, Aslan, & Powers. In this first experiment, we use the viscous parameter values utilized in the recent numerical study of Romick et al. [41]. Figure 4 shows that the smaller modulus roots enters for $\mathcal{E}_A \approx 2.75$ (Panel (a)) and the higher modulus roots for $\mathcal{E}_A \approx 3.65$ (Panel (d)). The high modulus roots have a turning point at about $\mathcal{E}_A \approx 5.2$, and the smaller modulus roots have theirs at $\mathcal{E}_A \approx 5.5$ (Panels (i) and (j) in Fig. 5). The large modulus roots leave at $\mathcal{E}_A \approx 6.55$ and the small modulus roots leave at approximately $\mathcal{E}_A \approx 6.85$ (Panel (n)).

Other than these two pairs, *there are no other roots in the nonstable half-plane* $\mathrm{Re}\,\lambda \geq 0$ other than the analytically determined simple translational eigenvalue at $\lambda = 0$ (excluded from our computations by taking inner radius 10^{-4}; for a proof of simplicity, see [36]). Indeed, at the spectral level the contrast with ZND is striking; see the right-hand panel in Figure 2 which shows the ZND spectra in a much larger portion of the unstable half plane than is shown in Figure 4. In Figure 2 the value of $\mathcal{E}_A$ is 7.1 which corresponds to just after panel (n) in the computation with viscosity. Notably, at this point in the computation with viscosity, the hyperstabilization has already taken place. In Table 1, we display the number of unstable roots and a bound on the modulus of unstable roots as activation energy increases.
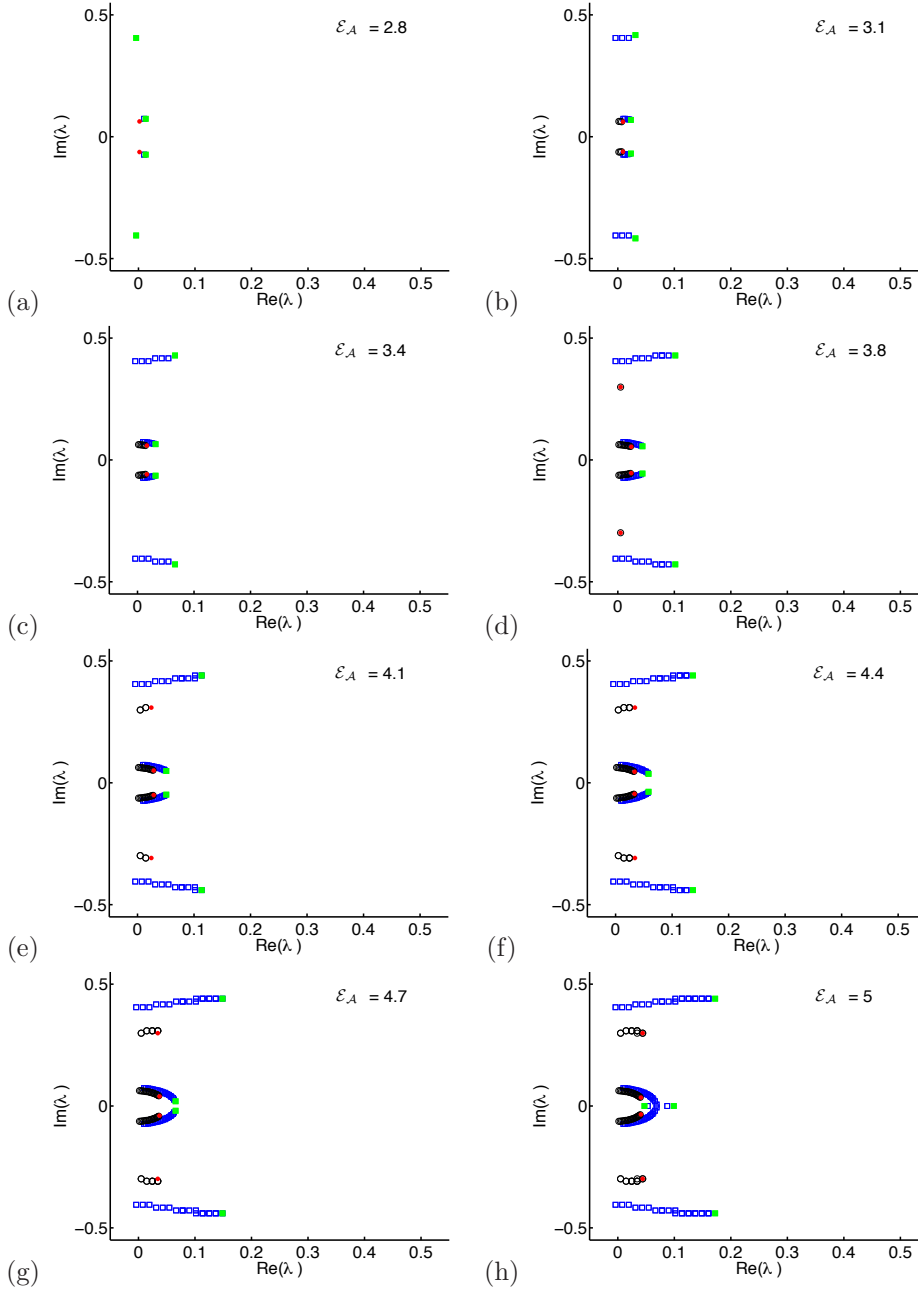
FIG. 4. *The movement of unstable roots in the complex plane as $\mathcal{E}_A$ increases. Circles (solid dot for current value of $\mathcal{E}_A$, open circles for previous values) mark the roots corresponding to the RNS model, while open squares (solid square for the current value of $\mathcal{E}_A$, open squares for previous values) correspond to the ZND model. The smaller modulus roots enters for $\mathcal{E}_A \approx 2.75$ (Panel (a)) and the higher modulus roots for $\mathcal{E}_A \approx 3.65$ (Panel (d)). The high modulus roots have a turning point at about $\mathcal{E}_A \approx 5.2$, and the smaller modulus roots have theirs at $\mathcal{E}_A \approx 5.5$ (Panels (i) and (j)—See Fig. 5). The large modulus roots leave at $\mathcal{E}_A \approx 6.55$ and the small modulus roots leave at approximately $\mathcal{E}_A \approx 6.85$ (Panel (n)). The other parameters are $\Gamma = 0.2$; $e_+ = 6.23e\text{-}2$; $q = 6.23e\text{-}1$; $D = 0.1$; $\kappa = 0.1$; $\nu = 0.1$; k chosen as described in §3.3; $\tau_- = 2.57e\text{-}1$; $u_- = 7.43e\text{-}1$; $e_- = 9.71e\text{-}1$; $c_v = 1$; $z_+ = 1$; $z_- = 0$; $\tau_+ = 1$; $u_+ = 0$; $s = 1$; $y_\pm = 0$; $T_+ = 6.2e\text{-}2$; $T_- = 9.71e\text{-}1$; and $T_{ig} = 6.64e\text{-}2$.*
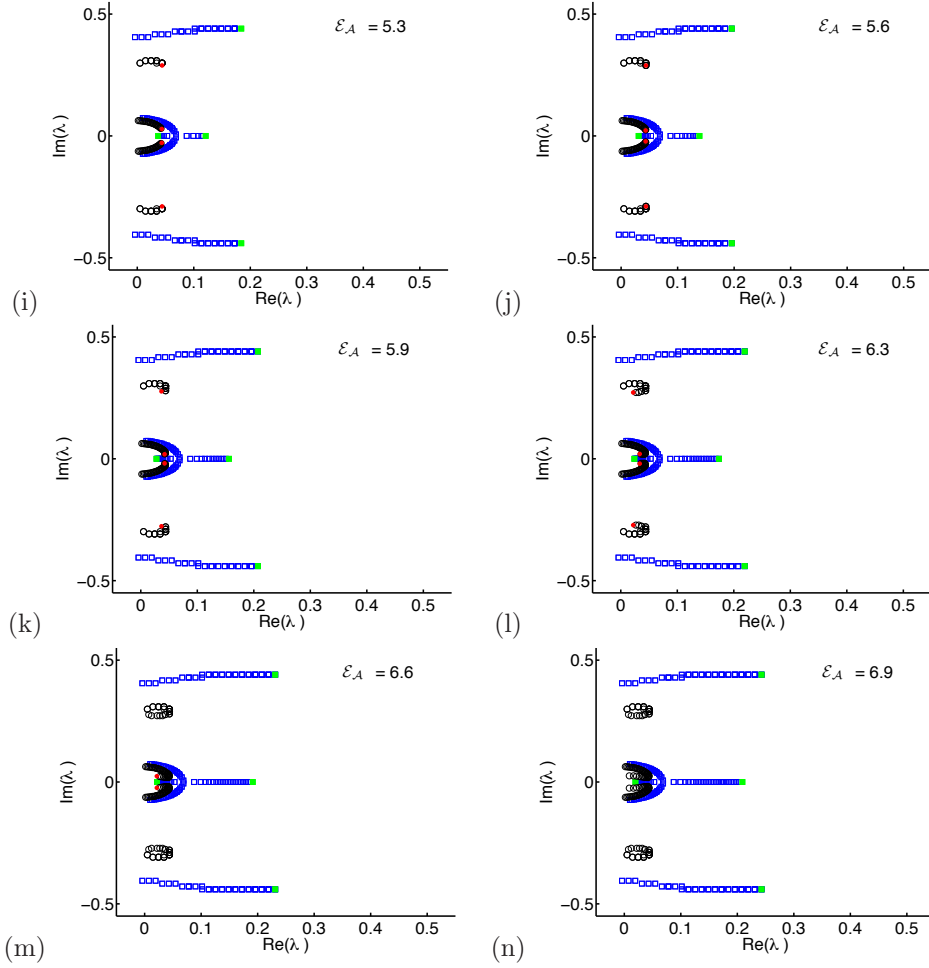
FIG. 5. *The movement of unstable roots in the complex plane as $\mathcal{E}_A$ increases (continued). See the description in the caption of Figure 4.*

6.2. Smaller viscosity. We see similar behavior even for smaller values of the viscous parameters; our experiments include viscous parameters one-half and one-fourth the size of those described in the previous subsection. Here, we find three and four complex conjugate pairs of eigenvalues crossing into the unstable half plane, but their behavior is the same—a return to stability. The smaller viscosity increases the level of $\mathcal{E}_A$ at which the return to stability occurs, but this growth seems to be slow; as noted below in §7, we see a further investigation of the growth of the upper stability boundary to be an important direction for further research.

REMARK 3 (Dependence on T_{ig}). *Our experiments show that raising T_{ig} seems to make roots turn back sooner (in $\mathcal{E}_A$). One possible explanation for this may be that moving T_{ig} and changing $\mathcal{E}_A$ do similar things to the shape of ϕ, roughly speaking.*

6.3. Lower and upper neutral stability boundaries. We found the hyperstabilization phenomenon for the entire range of viscosity parameters in our numerical experiments. That is, for fixed viscosity parameters, we see, as $\mathcal{E}_A$ increases, the emergence of complex-conjugate pairs of roots into the unstable half plane signaling

instability, and we also find, as $\mathcal{E}_A$ continues to increase, that these unstable roots return to the closed stable half plane. We denote by $\mathcal{E}_A^-$ the value of the *lower* neutral stability boundary (in advance of the appearance of unstable eigenvalues) and by $\mathcal{E}_A^+$ the value of the activation energy at which this return to neutral stability (no positive real part zeros of the Evans function) is achieved—the *upper* neutral stability boundary. Figure 1 shows a plot of the dependence of $\mathcal{E}_A^\pm$ on the strength of the viscosity. Notably, the figure shows that when the viscous effects are large enough, there is no instability. Indeed, Figure 3 illustrates the effect of viscous strength on the shape of the traveling-wave profiles. The right-hand figure (panel (b)) is computed at a viscosity value close to the "nose" in Figure 1 where the lower and upper boundaries coalesce. On the other hand, the left-hand figure (panel (a)) is computed near the inviscid ZND limit. As required, $\mathcal{E}_A^+$ increases as viscosity decreases [50]. Notably, however, the growth appears to be quite slow; this we see as an intriguing avenue for further investigation. In fact, the best-fit curve plotted in Figure 1 (dashed line) for the upper boundary includes a logarithmic term. By contrast, the behavior of the lower boundary seems to be much more regular. In this case, the best-fit curve (dashed line) for the relationship between $\mathcal{E}_A^-$ and ν is simply linear.

6.4. Computational effort. In carrying out our numerical investigations we used a 2009 MacBook with a 2.0 GHz Intel Core 2 Duo processor for code development and a Mac Pro with two Quad-Core Intel Xeon 2.26 GHz processors and the research cluster "Quarry" at Indiana University for time intensive computations. The software

TABLE 1

In this table, $\mathcal{E}_A$ indicates the activation energy, R indicates the bound of the modulus of any unstable roots as found via high-frequency curve fitting, and $\#$ indicates the number of roots of the Evans function found inside an annulus with outer radius R and inner radius $r = 10^{-4}$ via winding number computations with relative error between contour points no greater than 0.2. The other parameters are $\Gamma = 0.2$; $e_+ = 6.23e\text{-}2$; $q = 6.23e\text{-}1$; $D = 0.1$; $\kappa = 0.1$; $\nu = 0.1$; k chosen as described in §3.3; $\tau_- = 2.57e\text{-}1$; $u_- = 7.43e\text{-}1$; $e_- = 9.71e\text{-}1$; $c_v = 1$; $z_+ = 1$; $z_- = 0$; $\tau_+ = 1$; $u_+ = 0$; $s = 1$; $y_\pm = 0$; $T_+ = 6.2e\text{-}2$; $T_- = 9.71e\text{-}1$; and $T_{ig} = 6.64e\text{-}2$.

$\mathcal{E}_A$	2.0	2.1	2.2	2.3	2.4	2.5	2.6	2.7	2.8	2.9	3.0	3.1	3.2
$\#$	0	0	0	0	0	0	0	0	2	2	2	2	2
R	128	128	128	128	128	128	128	128	128	128	128	128	128
$\mathcal{E}_A$	3.3	3.4	3.5	3.6	3.7	3.8	3.9	4.0	4.1	4.2	4.3	4.4	4.5
$\#$	2	2	2	2	4	4	4	4	4	4	4	4	4
R	128	128	128	128	128	128	128	128	128	128	128	128	128
$\mathcal{E}_A$	4.6	4.7	4.8	4.9	5.0	5.1	5.2	5.3	5.4	5.5	5.6	5.7	5.8
$\#$	4	4	4	4	4	4	4	4	4	4	4	4	4
R	128	64	64	64	64	64	64	64	64	64	64	64	64
$\mathcal{E}_A$	5.9	6.0	6.1	6.2	6.3	6.4	6.5	6.6	6.7	6.8	6.9	7.0	7.1
$\#$	4	4	4	4	4	4	4	2	2	2	0	0	0
R	64	64	64	64	64	64	64	32	32	32	32	32	32
$\mathcal{E}_A$	7.2	7.3	7.4	7.5	7.6	7.7	7.8	7.9	8.0	8.1	8.2	8.3	8.4
$\#$	0	0	0	0	0	0	0	0	0	0	0	0	0
R	32	32	32	32	32	32	32	32	32	32	32	32	32
$\mathcal{E}_A$	8.5	8.6	8.7	8.8	8.9	9.0	9.1	9.2	9.3				
$\#$	0	0	0	0	0	0	0	0	0				
R	32	32	32	32	32	32	64	64	64				

TABLE 2

Upper neutral stability boundary: $\mathcal{E}_A^+(\nu)$. In most cases, we found the boundary with an absolute error of 0.05. For some values, we found the boundary with absolute error of 0.025; for those values we report more digits. Approximation of curves is carried out by bisection method, with error computed as the difference between the resulting bounding upper and lower values of $\mathcal{E}_A$.

ν	0.01	0.025	0.05	0.1	0.12	0.14	0.16	0.2
$\mathcal{E}_A^+$	9.25	8.6	7.75	6.85	6.65	6.35	6.15	5.75
ν	0.24	0.27	0.3	0.31	0.32	0.33	0.34	0.342
$\mathcal{E}_A^+$	5.35	5.1	4.8	4.65	4.55	4.375	4.225	4.125

TABLE 3

Lower neutral boundary: $\mathcal{E}_A^-(\nu)$. In most cases, we found the boundary with an absolute error of 0.05. For some values, we found the boundary with absolute error of 0.025; for those values we report more digits. Approximation of curves is carried out by bisection method, with error computed as the difference between the resulting bounding upper and lower values of $\mathcal{E}_A$.

ν	0.005	0.01	0.03	0.05	0.07	0.1	0.15	0.2
$\mathcal{E}_A^-$	2.45	2.45	2.55	2.65	2.65	2.75	2.85	3.05
ν	0.27	0.3	0.31	0.32	0.33	0.34	0.342	
$\mathcal{E}_A^-$	3.25	3.45	3.5	3.6	3.675	3.85	3.925	

environment consists of Matlab 2008 and newer.

We now provide some computational statistics to contrast the relative difficulty of our numerical investigations for ZND and RNS. For $\nu = 0.1$, $T_{\mathrm{ig}} = 0.99$, $\Gamma = 0.2$, $q = 0.623$, $e_+ = 0.062$, and $\mathcal{E}_A = 5$, it took 4.77 seconds to solve the RNS profile using the ZND profile as an initial guess in the bvp solver, whereas it took 1.69 seconds to solve the corresponding ZND profile (both on MacBook). It takes 13.7 minutes to solve for the roots of the Evans function shown in panel (h) of Figure 4, whereas it takes 24.7 seconds to solve the corresponding roots for ZND (8 cores on Mac Pro) .

To determine the stability boundaries, we used a bisection method wherein we adjust the lower or upper value of the interval enclosing the boundary based on the winding number of the Evans function or Evans–Lopatinskiĭ function (i.e., ZND Evans function) computed on a semi-circular contour. In computing the RNS lower stability boundary, we use the ZND stability boundary to get a good guess for an interval enclosing the boundary. For $\Gamma = 0.2$, $e_+ = 0.062$, $q = 0.221$, $T_{\mathrm{ig}} = 0.99$, and $\nu = 0.1$, it took 36.0 minutes to find the lower stability boundary within 0.05 relative error for RNS whereas it took 34.7 seconds to find the ZND lower stability boundary within 0.01 absolute error (8 cores on Mac Pro).

As the viscosity coefficients $\nu = D = \kappa \to 0$, the computation time increases in general. For example, to compute the RNS profile for small ν we had to use continuation in the boundary value solver with steps sometimes as small as 10^{-4} in either the viscosity coefficients $\nu = D = \kappa$ or in the activation energy $\mathcal{E}_A$. Computing the stability boundaries also required more time. For example, for $\Gamma = 0.2$, $e_+ = 0.062$, and $q = 0.331$, it took 1.02e4 seconds to find the RNS lower stability boundary for $\nu = 0.01$, 4.76e3 seconds for $\nu = 0.025$, 2.92e3 seconds for $\nu = 0.05$, and 2.06e3 seconds for $\nu = 0.1$. Overall, the most challenging aspect of this numerical study was the approximation of the traveling-wave profiles. Indeed, this was the limiting factor that determined the smallest viscosity we were able examine.

7. Discussion.

7.1. Findings. Our experiments indicate that viscous effects *can* be important in the stability analysis of detonation waves. First, we note that the inclusion of these effects delays the onset of instability; see the right-hand panel in Figure 1. We thus recover the results of Romick et al. [41], and we confirm that the effect of viscosity on $\mathcal{E}_A^-$ is essentially perturbative with a linear relationship between the value of $\mathcal{E}_A^-$ and the strength of viscosity. On the other hand, for all of the viscosity values tested, the difference between RNS and ZND *at the spectral level* is striking. Moreover, our results uncover the phenomenon of *viscous hyperstabilization*—a return to stability—as the bifurcation parameter (activation energy) increases. Now, as described above in §3.5, the broad range of viscosities considered in our experiments includes a physical range, starting with the fairly large viscosity considered by Romick et al. [41] and decreasing. Thus, it is of significant interest to determine whether or not the activation energies needed for complete stabilization also lie within a physically relevant range. For the viscosity level considered by Romick et al. [41], it is roughly twice the activation energy at which instability occurs for Fickett–Wood benchmark problem (7 vs. 3); for smaller viscosities, the level is successively larger, though the growth is surprisingly slow. It is not clear whether this size of activation energy might arise in physical situations. Nonetheless, even for much smaller activation energies, our results show that the spectra of viscous and inviscid waves differ profoundly. Now, Powers & Paolucci [39] have shown that a large range of length scales, including viscous length scales, are present in fully resolved models with realistic chemistry. Of course, the necessity of accounting for a large range of spatial/temporal scales depends very much on the problem at hand. But, the development of analytical and computational tools capable of dealing with such problems is of interest. For example, in more recent related work, Al-Khateeb et al. [1] discuss diffusive scales in the context of laminar flames, and Paolucci et al. [38] discuss and account for this range of scales in their development of adaptive methods appropriate for simulating compressible, reacting flow. Moreover, in terms of the stability of such waves, Bdzil & Stewart have identified "a better understanding of the hydrodynamic stability characteristics of our engineering-scale models" as one of four major challenges that must be met before a practically useful predictive theory for detonation phenomena can be constructed [9]. Combining these observations (scales, stability), we find motivation to develop a stability theory for detonation waves that incorporates diffusive effects. We see the present work, an Evans-based analysis, as an important step toward addressing this challenge.

7.2. Future directions. Several intriguing future directions for investigation have been identified in the body of this paper. Most notably, it would be of substantial mathematical and practical interest to carry out a singular perturbation analysis of the ZND limit and the restabilization seen here. It is known that the roots of the viscous Evans function converge to the roots of the limit ZND (inviscid) Evans–Lopatinskiǐ function [50], but a better understanding of viscous hyperstabilization and the corresponding growth of the upper stability boundary, as in Figure 1, is clearly needed. Another possibility would be to extend these calculations to more sophisticated models including, e.g., multiple space dimensions, multi-step chemistry, and more realistic equations of state; this is clearly necessary to answer the call of Bdzil & Stewart [9]. We note that for the Navier–Stokes equations of (nonreacting) gas dynamics, the extension of the STABLAB package to the multi-dimensional setting is underway. The incorporation of detailed chemical reaction processes provides an

excellent opportunity to test this computational suite on a problem of physical import.

Appendix A. Linearization: details. In this appendix, we provide for completeness the details of the linearization that is the basis for our computation of the Evans function. This calculation is the first step in the stability analysis, and there are a number of choices one must make to obtain a first-order eigenvalue ODE. A natural objective, then, is to determine which choices lead to the simplest, most useful formulation of the eigenvalue equation for our computational needs. Here, we follow the strategy of using *flux variables* (see (A.7)).

A.1. Preliminaries. We write the system (2.1) as

$$(A.1) \qquad f^0(U)_t + \left(f^1(U) - sf^0(U)\right)_x = \left(B(U)U_x\right)_x + R(U).$$

where $U = (\tau, u, e, z)^\top$. The functions f^0 and f^1 are given by

$$(A.2) \qquad f^0(U) = \begin{pmatrix} \tau & u & e + \frac{1}{2}u^2 & z \end{pmatrix}^\top, \quad f^1(U) = \begin{pmatrix} -u & p & up & 0 \end{pmatrix}^\top.$$

Also,

$$B(U) = \left(\begin{array}{c|ccc} 0 & 0 & 0 & 0 \\ \hline 0 & \frac{\nu}{\tau} & 0 & 0 \\ 0 & \frac{\nu u}{\tau} & \frac{\kappa_v}{\tau} & 0 \\ 0 & 0 & 0 & \frac{d}{\tau^2} \end{array}\right) = \begin{pmatrix} 0 & 0 \\ 0 & b(U) \end{pmatrix}, \quad R(U) = \begin{pmatrix} 0 \\ 0 \\ qk\phi(T(\tau, e, z))z \\ -k\phi(T(\tau, e, z))z \end{pmatrix}.$$

At this point we assume that the temperature T is a function of the internal energy, e, alone and does not depend on τ or z. This is certainly true in the fundamental case, $T = c_v^{-1}e$, that we consider in the calculations of this paper. We thus write $\check{\phi}(e) = \phi(T(e))$. This simplifies some of the calculations. Straightforward calculations show that

(A.3)

$$b(U)^{-1} = \begin{pmatrix} \frac{\tau}{\nu} & 0 & 0 \\ -\frac{\tau u}{\kappa_v} & \frac{\tau}{\kappa_v} & 0 \\ 0 & 0 & \frac{\tau^2}{d} \end{pmatrix}, \quad E(U) := dR(U) = \left(\begin{array}{c|ccc} 0 & 0 & 0 & 0 \\ \hline 0 & 0 & 0 & 0 \\ 0 & 0 & qk\check{\phi}'(e)z & qk\check{\phi}(e) \\ 0 & 0 & -k\check{\phi}'(e)z & -k\check{\phi}(e) \end{array}\right).$$

We also record here the forms of the Jacobian matrices $a^j = df^j$ for $j = 0, 1$. They are

$$(A.4) \quad a^0(U) := \left(\begin{array}{c|ccc} 1 & 0 & 0 & 0 \\ \hline 0 & 1 & 0 & 0 \\ 0 & u & 1 & 0 \\ 0 & 0 & 0 & 1 \end{array}\right) \quad \text{and} \quad a^1(U) := \left(\begin{array}{c|ccc} 0 & -1 & 0 & 0 \\ \hline p_\tau & 0 & p_e & p_z \\ up_\tau & p & up_e & up_z \\ 0 & 0 & 0 & 0 \end{array}\right).$$

We will utilize the block structure of the matrix B in our calculations.

A.2. Block structure. The linearized system of interest is given by

$$(A.5) \qquad \lambda a^0(x)W + \left(A(x)W - B(x)W'\right)' = E(x)W.$$

The unknown is $W = \begin{pmatrix} \tau & u & e & z \end{pmatrix}^\top$, with τ, u, e, z now representing (Laplace-transformed) perturbations. In (A.5), by a slight abuse of notation, we have written $a^0(x) = a^0(\bar{U}(x))$, $B(x) = B(\bar{U}(x))$, etc. Moreover,

$$A(x)W := [a^1(\bar{U}(x)) - sa^0(\bar{U}(x))]W - dB(\bar{U})(W, \bar{U}_x).$$

We will almost always suppress the dependence of the coefficients on x. Our aim is to write the eigenvalue problem (A.5) in the form of a first-order system (4.1). We write $W = \begin{pmatrix} W_1 & W_2 \end{pmatrix}^\top$ with $W_1 = \tau$ and $W_2 = \begin{pmatrix} u & e & z \end{pmatrix}^\top$, and we write the matrices A, B, and E in corresponding block form. That is, we write

$$(A.6) \qquad A = \begin{pmatrix} A_{11} & A_{12} \\ A_{21} & A_{22} \end{pmatrix},$$

so that A_{11} is 1×1, A_{12} is 1×3, A_{21} is 3×1, and A_{22} is 3×3, and we use the same block decomposition and notational conventions for the matrices B and E.

A.3. Flux variables. We define $Y = (Y_1, Y_2)^\top$ by $Y := AW - BW'$. When we rewrite this equation in terms of the blocks, we see

$$(A.7) \qquad \begin{pmatrix} Y_1 \\ Y_2 \end{pmatrix} = \begin{pmatrix} A_{11} & A_{12} \\ A_{21} & A_{22} \end{pmatrix} \begin{pmatrix} W_1 \\ W_2 \end{pmatrix} - \begin{pmatrix} 0 & 0 \\ 0 & b \end{pmatrix} \begin{pmatrix} W_1' \\ W_2' \end{pmatrix}.$$

Then, the vector $\mathcal{W}$ in (4.1) will be defined by $\mathcal{W} := \begin{pmatrix} Y & W_2 \end{pmatrix}^\top$. To extract the equations for Y_1', Y_2', and W_2', we note that the system (A.5) takes the block form

$$(A.8) \qquad \lambda \begin{pmatrix} a_{11}^0 & a_{12}^0 \\ a_{21}^0 & a_{22}^0 \end{pmatrix} \begin{pmatrix} W_1 \\ W_2 \end{pmatrix} + \begin{pmatrix} Y_1' \\ Y_2' \end{pmatrix} = \begin{pmatrix} E_{11} & E_{12} \\ E_{21} & E_{22} \end{pmatrix} \begin{pmatrix} W_1 \\ W_2 \end{pmatrix}.$$

Evidently, from the first row of (A.7), $Y_1 = A_{11}W_1 + A_{12}W_2$, whence

$$(A.9) \qquad W_1 = A_{11}^{-1}Y_1 - A_{11}^{-1}A_{12}W_2.$$

We'll see shortly that A_{11} is invertible. We shall use (A.9) to eliminate W_1 in favor of Y_1 and W_2 in the calculations that follow. From (A.8) and the fact that $E_{11} = 0$ and $E_{12} = 0$, it is clear that $\lambda(a_{11}^0 W_1 + a_{12}^0 W_2) + Y_1' = 0$. Inspection of (A.4) reveals that $a_{11}^0 = 1$, $a_{12}^0 = 0$. Therefore, using (A.9), we find

$$(A.10) \qquad Y_1' = \begin{bmatrix} -\lambda A_{11}^{-1} \end{bmatrix} Y_1 + \begin{bmatrix} 0 \end{bmatrix} Y_2 + \begin{bmatrix} \lambda A_{11}^{-1}A_{12} \end{bmatrix} W_2.$$

Similarly, we obtain an equation for Y_2'. The second row of (A.8) reads

$$\lambda(a_{21}^0 W_1 + a_{22}^0 W_2) + Y_2' = E_{21}W_1 + E_{22}W_2.$$

Again, several of the terms are zero. From (A.4) and the form of E, we see $a_{21}^0 = 0$, $E_{21} = 0$. Thus, we finally obtain

$$(A.11) \qquad Y_2' = \begin{bmatrix} 0 \end{bmatrix} Y_1 + \begin{bmatrix} 0 \end{bmatrix} Y_2 + \begin{bmatrix} E_{22} - \lambda a_{22}^0 \end{bmatrix} W_2.$$

All that remains is to derive an ODE for W_2. However, from (A.7) it is clear that

$$(A.12)$$
$$bW_2' = A_{21}W_1 + A_{22}W_2 - Y_2 = A_{21}A_{11}^{-1}Y_1 - Y_2 + \big(A_{21}(-A_{11}^{-1}A_{12}) + A_{22}\big)W_2.$$

Thus, from (A.12), we see that

$$(A.13) \qquad W_2' = \begin{bmatrix} b^{-1}A_{21}A_{11}^{-1} \end{bmatrix} Y_1 + \begin{bmatrix} -b^{-1} \end{bmatrix} Y_2 + \begin{bmatrix} b^{-1}(-A_{21}A_{11}^{-1}A_{12} + A_{22}) \end{bmatrix} W_2.$$

A.4. System & Evans function. We write the entries of the coefficient matrix G as

$$(A.14) \qquad G = \begin{pmatrix} g_{11} & g_{12} & g_{13} \\ g_{21} & g_{22} & g_{23} \\ g_{31} & g_{32} & g_{33} \end{pmatrix},$$

and we note that the entries of G can simply be read off from (A.10), (A.11), and (A.13). That is,

$$g_{11} = -\lambda A_{11}^{-1}, \qquad g_{12} = 0, \qquad g_{13} = \lambda A_{11}^{-1} A_{12},$$
$$g_{21} = 0, \qquad g_{22} = 0, \qquad g_{23} = E_{22} - \lambda a_{22}^0,$$
$$g_{31} = b^{-1} A_{21} A_{11}^{-1}, \qquad g_{32} = -b^{-1}, \qquad g_{33} = b^{-1}(-A_{21} A_{11}^{-1} A_{12} + A_{22}).$$

We now use the explicit forms of a^0, a^1, b, and E above to expand these entries. First, we note that, since the first row of B is zero, $A_{11} = a_{11}^1 - s a_{11}^0 = -s$, so that $A_{11}^{-1} = -\frac{1}{s}$. We recall that we require $s \neq 0$. Also, $A_{12} = a_{12}^1 - s a_{12}^0 = (-1 \quad 0 \quad 0)$. Thus, the entries in the first row of G are

$$g_{11} = \lambda/s, \quad g_{12} = (0 \quad 0 \quad 0), \quad g_{13} = (\lambda/s \quad 0 \quad 0).$$

Similarly, we see that the entries in the second row of G are

$$g_{21} = \begin{pmatrix} 0 \\ 0 \\ 0 \end{pmatrix}, \quad g_{22} = \begin{pmatrix} 0 & 0 & 0 \\ 0 & 0 & 0 \\ 0 & 0 & 0 \end{pmatrix}, \quad g_{23} = \begin{pmatrix} -\lambda & 0 & 0 \\ -\lambda u & -\lambda + qk\check{\phi}'(e)z & qk\check{\phi}(e) \\ 0 & -k\check{\phi}'(e)z & -\lambda - k\check{\phi}(e) \end{pmatrix}.$$

Finally, it remains to compute the entries in the third row. We start by calculating the two lower blocks of A. They are

$$(A.15)$$
$$A_{21} = \begin{pmatrix} p_\tau + \dfrac{\nu u_x}{\tau^2} \\ p_\tau u + \dfrac{\nu u u_x}{\tau^2} + \dfrac{\kappa_v e_x}{\tau^2} \\ 2\dfrac{D z_x}{\tau^3} \end{pmatrix} \quad \text{and} \quad A_{22} = \begin{pmatrix} -s & p_e & p_z \\ -su + p - \dfrac{\nu u_x}{\tau} & -s + u p_e & u p_z \\ 0 & 0 & -s \end{pmatrix}.$$

Then,

$$(A.16) \qquad g_{31} = b^{-1} A_{21} A_{11}^{-1} = \begin{pmatrix} \dfrac{\tau p_\tau}{\nu} + \dfrac{u_x}{\tau} \\ \dfrac{e_x}{\tau} \\ \dfrac{2 z_x}{\tau} \end{pmatrix} (-1/s).$$

Also, from (A.3), we see immediately that

$$(A.17) \qquad g_{32} = - \begin{pmatrix} \dfrac{\tau}{\nu} & 0 & 0 \\ -\dfrac{\tau u}{\kappa_v} & \dfrac{\tau}{\kappa_v} & 0 \\ 0 & 0 & \dfrac{\tau^2}{D} \end{pmatrix}.$$

Finally, we compute

$$g_{33} = b^{-1}(-A_{21}A_{11}^{-1}A_{12} + A_{22}) = \begin{pmatrix} \frac{\tau}{\nu}\mathbf{c}_1 & \frac{\tau}{\nu}p_e & \frac{\tau}{\nu}p_z \\ -\frac{\tau u}{\kappa_v}\mathbf{c}_1 + \frac{\tau}{\kappa_v}\mathbf{c}_2 & -p_e\frac{\tau u}{\kappa_v} - s\frac{\tau}{\kappa_v} + \frac{\tau}{\kappa_v}up_e & 0 \\ \frac{\tau^2}{D}\mathbf{c}_3 & 0 & -s\frac{\tau^2}{D} \end{pmatrix}$$

with

$$\mathbf{c}_1 = -\frac{1}{s}\left(p_\tau + \frac{\nu u_x}{\tau^2}\right) - s\,, \mathbf{c}_2 = -\frac{1}{s}\left(p_\tau u + \frac{\nu u u_x}{\tau^2} + \frac{\kappa_v e_x}{\tau^2}\right) - su + p - \frac{\nu u_x}{\tau}\,,$$
$$\mathbf{c}_3 = -\frac{1}{s}\left(2D\frac{z_x}{\tau^3}\right)\,.$$

This completes the derivation of the entries in the coefficient matrix G in (4.1).

Acknowledgement: The authors thank Mark Williams for helpful conversations concerning the existence of detonation profiles in the inviscid limit.

REFERENCES

[1] A. N. AL-KHATEEB, J. M. POWERS, AND S. PAOLUCCI, *Analysis of the spatio-temporal scales of laminar premixed flames near equilibrium*, Combustion Theory and Modelling, 17 (2013), pp. 76–108.

[2] J. C. ALEXANDER AND R. SACHS, *Linear instability of solitary waves of a Boussinesq-type equation: a computer assisted computation*, Nonlinear World, 2 (1995), pp. 471–507.

[3] L. ALLEN AND T. BRIDGES, *Numerical exterior algebra and the compund matrix method*, Numer. Math., 92 (2002), pp. 197–232.

[4] B. BARKER, J. HUMPHERYS, K. RUDD, AND K. ZUMBRUN, *Stability of viscous shocks in isentropic gas dynamics*, Comm. Math. Phys., 281 (2008), pp. 231–249.

[5] B. BARKER, J. HUMPHERYS, AND K. ZUMBRUN, *STABLAB: A MATLAB-based numerical library for Evans function computation*, 2009.

[6] B. BARKER, M. A. JOHNSON, P. NOBLE, L. M. RODRIGUES, AND K. ZUMBRUN, *Nonlinear modulational stability of periodic traveling-wave solutions of the generalized Kuramoto-Sivashinsky equation*, Phys. D, 258 (2013), pp. 11–46.

[7] B. BARKER AND K. ZUMBRUN, *A numerical investigation of stability of ZND detonations for Majda's model*, 2010. Preprint (arXiv:1011.1561).

[8] ———, *Numerical stability analysis of ZND detonations*, 2014. In preparation.

[9] J. B. BDZIL AND D. S. STEWART, *The dynamics of detonation in explosive systems*, Annual Rev. Fluid Mech., 39 (2007), pp. 263–292.

[10] A. BOURLIOUX, A. J. MAJDA, AND V. ROYTBURD, *Theoretical and numerical structure for unstable one-dimensional detonations*, SIAM J. Appl. Math., 51 (1991), pp. 303–343.

[11] T. J. BRIDGES, G. DERKS, AND G. GOTTWALD, *Stability and instability of solitary waves of the fifth-order kdv equation: a numerical framework*, Phys. D, 172 (2002), pp. 190–216.

[12] L. Q. BRIN, *Numerical testing of the stability of viscous shock waves*, Math. Comp., 70 (2001), pp. 1071–1088.

[13] L. Q. BRIN AND K. ZUMBRUN, *Analytically varying eigenvectors and the stability of viscous shock waves*, Mat. Contemp., 22 (2002), pp. 19–32. Seventh Workshop on Partial Differential Equations, Part I (Rio de Janeiro, 2001).

[14] J. C. BRONSKI, *Semiclassical eigenvalue distribution of the Zakharov-Shabat eigenvalue problem*, Phys. D, 97 (1996), pp. 376–397.

[15] G.-Q. CHEN, *Global solutions to the compressible Navier-Stokes equations for a reacting mixture*, SIAM J. Math. Anal., 23 (1992), pp. 609–634.

[16] P. COLELLA, A. MAJDA, AND V. ROYTBURD, *Theoretical and numerical structure for reacting shock waves*, SIAM J. Sci. Statist. Comput., 7 (1986), pp. 1059–1080.

[17] R. COURANT AND K. O. FRIEDRICHS, *Supersonic flow and shock waves*, Springer-Verlag, 1976. Reprinting of the 1948 original; Applied Mathematical Sciences, Vol. 21.

[18] J. J. ERPENBECK, *Stability of steady-state equilibrium detonations*, Phys. Fluids, 5 (1962), pp. 604–614.

[19] ———, *Stability of idealized one-reaction detonations*, Phys. Fluids, 7 (1964), pp. 684–696.

[20] W. Fickett and W. Davis, *Detonation: Theory and Experiment*, Dover, 2000. corrected reprint of 1979 UC Berkeley Edition.

[21] W. Fickett and W. W. Wood, *Flow calculations for pulsating one-dimensional detonations*, Phys. Fluids, 9 (1966), pp. 903–916.

[22] R. A. Gardner, *On the detonation of a combustible gas*, Trans. Amer. Math. Soc., 277 (1983), pp. 431–468.

[23] I. Gasser and P. Szmolyan, *A geometric singular perturbation analysis of detonation and deflagration waves*, SIAM J. Math. Anal., 24 (1993), pp. 968–986.

[24] J. Hendricks, J. Humpherys, G. Lyng, and K. Zumbrun, *Stability of viscous weak detonations for majda's model*, J. Dynam. Diff. Eqs., (2013). submitted.

[25] D. Henry, *Geometric theory of semilinear parabolic equations*, vol. 840 of Lecture Notes in Mathematics, Springer-Verlag, 1981.

[26] J. O. Hirschfelder and C. F. Curtiss, *Theory of detonations. I. Irreversible unimolecular reaction*, J. Chem. Phys., 28 (1958), pp. 1130–1147.

[27] J. Humpherys, G. Lyng, and K. Zumbrun, *Spectral stability of ideal-gas shock layers*, Arch. Ration. Mech. Anal., 194 (2009), pp. 1029–1079.

[28] ———, *Stability of viscous detonations for Majda's model*, Phys. D, 259 (2013), pp. 63–80.

[29] J. Humpherys, B. Sandstede, and K. Zumbrun, *Efficient computation of analytic bases in Evans function analysis of large systems*, Numer. Math., 103 (2006), pp. 631–642.

[30] J. Humpherys and K. Zumbrun, *An efficient shooting algorithm for Evans function calculations in large systems*, Phys. D, 220 (2006), pp. 116–126.

[31] ———, *Efficient numerical stability analysis of detonation waves in ZND*, Quart. Appl. Math., 70 (2012), pp. 685–703.

[32] H. K. Jenssen, G. Lyng, and M. Williams, *Equivalence of low-frequency stability conditions for multidimensional detonations in three models of combustion*, Indiana Univ. Math. J., 54 (2005), pp. 1–64.

[33] T. Kato, *Perturbation theory for linear operators*, Classics in Mathematics, Springer-Verlag, 1995. Reprint of the 1980 edition.

[34] H. I. Lee and D. S. Stewart, *Calculation of linear detonation instability: one-dimensional instability of plane detonation*, J. Fluid Mech., 216 (1990), pp. 103–132.

[35] G. Lyng, M. Raoofi, B. Texier, and K. Zumbrun, *Pointwise green function bounds and stability of combustion waves*, J. Differential Equations, 233 (2007), pp. 654–698.

[36] G. Lyng and K. Zumbrun, *One-dimensional stability of viscous strong detonation waves*, Arch. Ration. Mech. Anal., 173 (2004), pp. 213–277.

[37] B. S. Ng and W. H. Reid, *The compound matrix method for ordinary differential systems*, J. Comput. Phys., 58 (1985), pp. 209–228.

[38] S. Paolucci, Z. J. Zikoski, and D. Wirasaet, *WAMR: An adaptive wavelet method for the simulation of compressible reacting flow. part i. accuracy and efficiency of algorithm*, Journal of Computational Physics, 272 (2014), pp. 814 – 841.

[39] J. M. Powers and S. Paolucci, *Accurate spatial resolution estimates for reactive supersonic flow with detailed chemistry*, AIAA J., 43 (2005), pp. 1088–1099.

[40] C. M. Romick, T. D. Aslam, and J. D. Powers, *The dynamics of unsteady detonation with diffusion*, AIAA, (2011).

[41] C. M. Romick, T. D. Aslam, and J. M. Powers, *The effect of diffusion on the dynamics of unsteady detonations*, J. Fluid Mech., 699 (2012), pp. 453–464.

[42] B. Sandstede, *Stability of travelling waves*, in Handbook of dynamical systems, Vol. 2, North-Holland, Amsterdam, 2002, pp. 983–1055.

[43] D. S. Stewart and A. R. Kasimov, *State of detonation stability theory and its application to propulsion*, J. of Propulsion and Power, 22 (2006), pp. 1230–1244.

[44] D. Tan and A. Tesei, *Nonlinear stability of strong detonation waves in gas dynamical combustion*, Nonlinearity, 10 (1997), pp. 355–376.

[45] B. Texier and K. Zumbrun, *Transition to longitudinal instability of detonation waves is generically associated with Hopf bifurcation to time-periodic galloping solutions*, Comm. Math. Phys., 302 (2011), pp. 1–51.

[46] F. A. Williams, *Combustion Theory*, Westview Press, 2 ed., 1985.

[47] M. Williams, *Heteroclinic orbits with fast transitions: a new construction of detonation profiles*, Indiana Univ. Math. J., 59 (2010), pp. 1145–1209.

[48] K. Zumbrun, *Stability of large-amplitude shock waves of compressible Navier-Stokes equations*, in Handbook of mathematical fluid dynamics. Vol. III, North-Holland, Amsterdam, 2004, pp. 311–533. With an appendix by H. K. Jenssen and G. Lyng.

[49] ———, *Numerical error analysis for Evans function computations: a numerical gap lemma,*

centered-coordinate methods, and the unreasonable effectiveness of continuous orthogonal-ization, 2009. arXiv:0904.0268.

[50] ———, Stability of detonation profiles in the ZND limit, Arch. Ration. Mech. Anal., 200 (2011), pp. 141–182.